State-of-the-art multimodal scanning hard X-ray imaging and tomography sheds light at multiple length-scales on biomineralization related processes

K. Medjoubi[1]*[†], K. Benzerara[2], J. Debrie[2], E. Tang[3], D. Bazin[4],
E. Letavernier[3], K. Desjardins[1] and A. Somogyi[1]*[†]

[1]Synchrotron Soleil, Saint-Aubin, France, [2]Institut de Minéralogie de Physique Des Matériaux Et de
Cosmochimie, Sorbonne Université, UMR7590, CNRS, Muséum National D'Histoire Naturelle, Paris,
France, [3]Sorbonne University and Tenon Hospital (AP-HP), Paris, France, [4]CNRS Institute of Physical
Chemistry, Orsay, France

Biomineralization is a widespread process among living organisms, playing a significant role in the formation and preservation of geological structures, biogeochemical cycles, regulation of ocean chemistry, and carbon sequestration. Moreover pathological biomineralization has a huge impact on human health. The growth of biominerals provides a rich area for research at multiple length-scales since they have controlled hierarchical structures from nano-to macroscopic scales. Here, we provide an overview on the potentials of the state-of-the-art scanning hard X-ray imaging and tomography methods developed at the NANOSCOPIUM beamline at Synchrotron Soleil in such studies. Multimodal scanning imaging provides simultaneous information on the elemental composition by X-ray fluorescence (XRF) spectrometry, on the sample morphology by absorption contrast imaging, on the crystalline structure by X-ray diffraction, and on the luminescence characteristics by X-ray Excited Optical Luminescence. As illustrated through diverse research cases about biomineralization in stromatolites and pathological calcification, such a versatile portfolio of X-ray imaging techniques provides unique complementary information to conventional laboratory techniques on biominerals and the underlying mineral precipitation processes.

KEYWORDS

biomineralization, stromatolites, pathological calcification, scanning hard X-ray imaging and tomography, multi-length-scale, multimodal, trace metals

1 Introduction

Biomineralization is the biological formation of mineral structures. Biomineralization is an extremely widespread process among living organisms throughout all taxonomic clades. As such, it plays a significant role in, e.g., the formation and preservation of geological structures, including marine sediments, biogeochemical cycles, regulation of ocean chemistry, and carbon sequestration. Since the process of biomineralization and the incorporation of trace elements is affected by environmental parameters (e.g.,

temperature, salinity, pH, ionic composition of the surrounding medium), biominerals can also serve as potential paleo-proxies by archiving environmental changes if biological and environmental effects on mineral formation can be untangled. Pathological biomineralization (Bazin et al., 2012; Bazin et al., 2016) including, e.g., osteo-porosis, osteo-malacia, kidney stones, and atherosclerosis, have a huge impact on human health. Consequently, understanding the mechanisms controlling biomineralization and identifying inorganic processes influencing the composition of the biominerals have important implications in tackling several of the great scientific challenges of the forthcoming decades and to decipher long-term history of changes in the environmental conditions and evolution of life on Earth and other planets.

Yet, biomineralization mechanisms are not fully understood. The study of biomineralization is an intrinsically interdisciplinary research field at the crossroads of biology, chemistry, medicine, exobiology, geo-biochemistry, material science and environmental sciences. The growth of biominerals provides a rich area for research at multiple length-scales, since they have controlled hierarchical structures from nano-to macroscopic scales, multifunctional properties, and remarkable optical and mechanical features. Characterizing changes in contents, spatial distributions, and speciation of the elements is therefore essential for understanding mechanisms required to prevent or cure diseases.

Emerging analytical tools, such as multi-modal scanning hard X-ray imaging (e.g. (Somogyi et al., 2015; Schroer et al., 2016; Yan et al., 2016; Martínez-Criado et al., 2017; Parsons et al., 2017; Suuronen and Sayab, 2018; Yan et al., 2018; Chu et al., 2020; Quinn et al., 2021; Callefo et al., 2022; NANOSCOPIUM, 2024)) can provide invaluable pieces of information about these highly heterogenous hierarchical structures at multiple length-scales in 2D and/or 3D, offering new insights on biomineral formation pathways. Here, we provide an overview of the possibilities offered by such multimodal and multi-length-scale scanning X-ray imaging and tomography methods, through research examples performed at the NANOSCOPIUM beamline at synchrotron SOLEIL. At NANOSCOPIUM the implementation of a user-friendly semiautomatic imaging and tomography workflow (Guo et al., 2022) permits the on-the-fly tuning of the multimodal and multi-length-scale experiments. The new potentials opened by these state-of-the-art X-ray imaging methods by providing simultaneous information on the elemental composition by X-ray fluorescence (XRF) spectrometry, on the morphology by absorption contrast imaging, on the crystalline structure by X-ray diffraction (XRD), and on the luminescence characteristics by X-ray Excited Optical Luminescence (XEOL) are illustrated through diverse research cases about biomineralization in stromatolites (one of the oldest known fossils on Earth), and pathological calcification.

2 Materials and methods

2.1 The NANOSCOPIUM scanning hard X-ray imaging beamline

The synchrotron imaging experiments presented in this work have been performed at the NANOSCOPIUM scanning hard X-ray
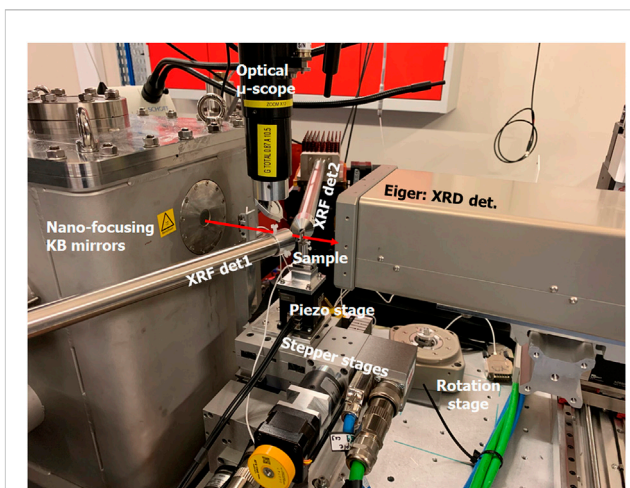

FIGURE 1
The Kirkpatrick Baez-mirror (KB) based end-station of the NANOSCOPIUM beamline shown with the experimental set-up of simultaneous scanning XRD and XRF 2D projection imaging. The KB mirrors are situated in the vacuum vessel. The direction of the focused beam behind the Be exit window of the KB vacuum chamber is indicated by the red arrow. The shown sample scanning stage contains two stepper stages at the bottom and a 2-axis (nPoint) piezo stage on the top. The sample is positioned onto the sample stage using a magnetic sample holder. The optical microscope permits straightforward sample alignment into the focused nano-beam. The two SDD XRF detectors are situated symmetrically around the sample. The 2D photon counting pixel detector (Eiger) used to record the XRD patterns is installed behind the sample. For scanning tomography experiments the piezo stages are replaced by an air-bairing rotation stage (visible behind the projection imaging set-up) on the top-of the stepper motor-stages.

nanoprobe beamline at Synchrotron Soleil, St Aubin, France (Somogyi et al., 2015; NANOSCOPIUM, 2024). NANOSCOPIUM uses monochromatic X-rays for probing the sample characteristics by multimodal and multi-length-scale imaging techniques. The X-ray energy can be tuned by a double crystal Si (111) monochromator in the 5–20 keV energy range with a $\Delta E/E \sim 10^{-4}$ energy resolution.

The measurements presented in this paper were performed at the Kirkpatrick-mirror (KB) based end-station of the beamline (see Figure 1), where the size of the focused beam can be tailored, without beamline realignment, in the 70 nm–500 nm range to match the experimental requirements. The nano-focusing KB mirrors (JTEC) are situated in medium (10^{-7} mbar) vacuum. An extractible optical microscope installed between the KB mirror and the sample is used for aligning the sample into the focus plane of the KB mirror. For scanning 2D projection imaging the samples are mounted on a scanning stage containing two stepper motors at the bottom for coarse scanning with 0.4–1 µm pixel size, and a 2-axis piezo stage (nPCube, Motion Solution inc) on the top for high, 50–400 nm, resolution scanning. For XRF tomography acquisitions the samples are mounted onto an air-bairing rotation stage (visible in Figure 1 behind the 2D projection imaging set-up) replacing the piezo stages, permitting to achieve down to 400 nm voxel size in scanning tomography experiments.

All scanning imaging/tomography experiments are performed by using continuous sample scanning (FLYSCAN) developed at Synchrotron Soleil (Medjoubi et al., 2013). The fast continuous

scanning possibility and the easily adjustable focused beam size at the sample position provide straightforward access to multi-length-scale imaging of mesoscale samples both in 2D and 3D on the very same sample stage, with no need for beamline realignment nor for sample repositioning. A fast (down to some ms/pixel dwell time) scanning of large, up to 1 mm² sample regions with 1 µm pixel size provides a large overview scan, from which some tens of µm regions are chosen for high-resolution mapping.

The samples are measured in air at ambient conditions. This provides a straightforward access to multimodal imaging by implementing X-ray Fluorescence (XRF), X-ray Absorption Near Edge Spectroscopy (XANES), X-ray Diffraction (XRD), X-ray Excited Optical Luminescence (XEOL), and absorption contrast by introducing dedicated detectors around the sample. Moreover, an intensity monitor (8 µm thick silicon diode) is situated in the beam-path upstream of the KB-mirrors to measure the intensity of the incoming X-ray beam. In each pixel of the measured images a hardware trigger assures the synchronized collection of each detector and the absolute position of each scanning linear and rotation sample stage.

2.2 Scanning X-ray imaging techniques available at NANOSCOPIUM

2.2.1 Scanning absorption contrast imaging and tomography

The absorption contrast has been measured by introducing a 300 µm thick silicon diode behind the sample. The absorption within the sample is calculated in each pixel from the measured incoming and transmitted beam intensities for absorption contrast imaging and tomography.

2.2.2 X-ray fluorescence spectroscopy

The elemental distribution of the sample was measured by X-ray fluorescence spectrometry by introducing two silicon drift diode detectors (SDD, VITUS H50, KETEK GmbH) at ~75° to the incident beam direction to increase the detection angle. Full XRF spectra have been collected in each image pixel. The sum-spectra of the analyzed sample areas have been fitted with the PyMCA 4.6.0 software (Solé et al., 2007). The distribution maps of the elements identified from the sum-spectra were created by a homemade MATLAB code including deadtime, measurement time, and spectral overlapping correction. Semi-quantification of the detected elements was performed by using the AXO thin film XRF reference sample for calibration (AXO, 2024). The high analytical sensitivity of synchrotron radiation induced nano-X-ray fluorescence spectrometry (nano-SR-XRF) permits to detect trace elements down to ppm concentrations at NANOSCOPIUM.

2.2.3 X-ray diffraction

The presence and distribution of the crystalline phases were measured by nano-X-ray diffraction (XRD) simultaneously with nano-XRF (see Figure 1). A diffraction pattern has been collected in each pixel in transmission mode by using a 2D single photon counting X-ray pixel detector provided by the detector group of the Swiss synchrotron SLS (Tinti et al., 2015). It covers an area of 4 cm × 8 cm with a pixel size of 75 µm. High counting rate (up

to ~5 × 10⁵ photons/s/pixel) and high frame rate (kHz range) capabilities make it particularly suitable for fast scanning nano-diffraction experiments. The detector is placed 4.5 cm downstream of the sample perpendicular to the X-ray beam axis. A beam-stop allows to absorb the direct beam to protect the detector from radiation damage. An azimuthal integration of each XRD image was performed by a homemade MATLAB code to obtain the conventional Intensity vs. 2Θ diffractograms at each position on the sample. The crystalline phases were identified using the "Match!—Phase Analysis using Powder Diffraction" Version 3 × software (Putz and Brandenburg, 2024). The intensity of a given diffraction peak of the diffractogram is used to map the intensity variation of a given hkl reflection. Information on the preferential orientations of the crystallites can be also extracted by measuring the intensity profile of a hkl reflection along the azimuthal angle. In order to increase the signal to noise ratio of the diffractograms, hkl profiles or 2D XRD patterns measured in individual pixels of the map can be summed within a region of interest chosen from any other simultaneously obtained imaging modality.

2.2.4 X-ray excited optical luminescence

X-ray excited optical luminescence (XEOL) is a photon-in/photon-out technique, in which core electron levels are excited by X-rays and the emitted fluorescence (Sham, 2014; Gaft et al., 2015) is detected in the [UV, IR] range. The wavelength of the photons emitted during the deactivation of the sample depends among others on the chemical composition and crystalline structure of the sample, and the presence of activator or inhibitor elements, which are usually present in trace quantity. Indeed, the emitted luminescence signal is particularly sensitive to the presence and preservation of organic molecules and to the presence of trace elements captured in the minerals. The XEOL setup installed at NANOSCOPIUM consisted of a ×10 microscope objective (Thorlabs, Inc.) to collect the emitted luminescence, a filter wheel with 9 bandpass filters, each having a 50 nm-wavelength width, for wavelengths selection in the 350 nm and 675 nm wavelength range (Thorlabs, Inc.), and a photomultiplier (Hamamatsu module H7722-40). The 10th position in the wheel, which is empty, allows to collect the full emitted luminescence spectrum. During the XEOL measurements of the stromatolite samples, the luminescence signal was acquired in the 625 nm and 675 nm (red luminescence) wavelength range. XEOL and XRF imaging have been performed simultaneously with 40 ms/pixel integration time. The XEOL distribution map was created using a homemade MATLAB code.

2.2.5 Scanning multimodal absorption contrast-, XRF-, XRD-, and XEOL-imaging

The multimodal scanning imaging and tomography experiments, including any combination of XRF, XRD, and Absorption Contrast imaging/tomography, and XEOL-imaging, are performed on the very same sample stage and sample load by introducing the appropriate detectors around the sample. All detectors required for these analytical modalities are mounted on motorized detector positioning stages. This permits the fast and reproducible positioning of any detector-combination around the sample with no beamline realignment nor sample repositioning/reloading. Moreover, each detector is incorporated into the Flyscan

architecture for simultaneous data-collection in each image pixel by using a hardware trigger for synchronization. This results in an integrated multimodal dataset, including the absolute position of each scanning linear and rotation sample stage, where the different image modalities can be merged directly. In the current experimental setup, the interchange of two detectors is only necessary if both the XEOL and XRD techniques are used during a multimodal imaging experiment, since these two detectors are used in transmission geometry behind the sample. To assure the easy integration of these two sequentially measured modalities into a common integrated multimodal dataset, XRF imaging is performed simultaneously with each of them.

2.2.6 Sparse and high-resolution scanning X-ray tomography

All scanning tomography measurements of the mouse renal papillae samples have been performed over 360°. During these time-consuming experiments, a reasonable trade-off must be reached regarding acquisition time, spatial resolution, and the number of samples wished to be analyzed. The total measurement time of a tomography experiment scales proportionally with the number of angular projections; thus, it can be drastically reduced by performing sparse tomography with limited number of angular projections. The figure of merit of sparse tomography is to identify, within acceptable measurement time and medium resolution, the features of interest. In the case of renal papillae samples, the presence and distribution of Ca-rich early pathological calcifications, the elements linked to them, and their mineralogical phases could be identified in tissular context. The spatial resolution of the reconstructed sparse tomograms improves with the number of angular projections. As such, the measured projection number can be tuned to match the size of the features of interest. According to the estimation we obtained by Fourier ring correlation (FRC) analysis (van Heel and Schatz, 2005), measuring 20 angular projections over 360° permits to obtain 8.4 μm spatial resolution of the reconstructed tomograms of a renal papillae sample of 500–700 μm dimensions. This can be pushed down to 5.4 μm in case of measuring 40 angular projections at the cost of doubling the total measurement time. For our study, the best-balanced scanning parameters to obtain an optimal trade-off between total measurement time and spatial resolution were 20 projection angles with 2 μm lateral pixel size, and 20 ms/pixel exposure time. This provided good quality medium-resolution tomograms for sparse XRF and complementary multimodal tomographies in a couple of hours (3–5 h), by using the maximum-likelihood expectation–maximization (MLEM) reconstruction algorithm (Hunter and Lange, 2004; Pafilis et al., 2011). The MLEM algorithm results in a significant resolution improvement compared to the spatial resolution given by the Nyquist sampling condition (Epstein, 2008) (see details in (Guo et al., 2022)). The reconstructed sparse tomograms allow choosing the altitude(s) for high-resolution (HR) single slice tomography, which were performed by measuring 360 angular projections over 360° resulting in ~1 μm spatial resolution. The above-described measurement strategy permitted to optimize the scanning tomography experiments within 5 days, the typical duration of a user experiment at NANOSCOPIUM.

Three Characteristic 2D/3D features identified from the multimodal projection images or 2D/3D tomograms were further analyzed on-site or post-experiment by PyMCA (Solé et al., 2007) for XRF data processing, by ImageJ (Schindelin et al., 2012) and MATLAB for image processing and integrated imaging, and by Chimera (Pettersen et al., 2004) for volume rendering and visualization of the reconstructed multimodal tomograms.

3 Results

Study of Biomineralization by Scanning Multimodal Hard X-ray Imaging.

3.1 Stromatolites

Stromatolites are laminated organo-sedimentary rocks, originating from biologically induced, influenced, and controlled precipitation of mostly carbonate minerals (Görgen et al., 2021). Their formation involves repeated successive mineral precipitation events and microbial growth resulting in their characteristic laminated structure. Stromatolites are among the oldest known traces of life on Earth documented for more than 3.5 billion years and they are omnipresent in the fossil record (Bosak et al., 2013). Modern, actively growing stromatolites usually contain diverse microbial communities, including abundant phototrophs covering the mineral component (Iniesto et al., 2021). Since they are preserving the traces of life-mineral interactions since deep geological times up to now, they provide precious information about the geobiological history of the Earth. The major difficulty when studying ancient stromatolites is to assess the post-depositional transformations that they experienced over time which result, in particular, in a partial or total degradation of organic matter, for example, obscuring their biological origin. A usual approach followed by specialists of this field consist in thoroughly characterizing the morphology of the rocks, their chemical and mineralogical composition, and assessing the presence of microfossils, which can all be linked to some extent to past biological activities.

Studying modern stromatolites is a valuable approach to understand processes that formed ancient microbialites and better interpret traces left by life in minerals. Here, we present the study of modern stromatolites from the coastal Mari Ermi lagoon on the west coast of Sardinia. These stromatolites provide a particularly interesting case of study since they experience severe variations of their chemical environment, especially its salinity, with a water chemistry close to that of seawater in the winter and complete drying of the lagoon in the summer (Saint Martin and Saint Martin, 2015). We aim to understand the impact of microorganisms on the mineralogical and chemical composition of the stromatolites. Based on laboratory, mostly electron microscopy-based, analyses, these highly heterogenous laminated structures were shown to contain local variations of the Mg content of calcite spatially associated with remnants of microbial cells (Debrie et al., 2022). Here, we used scanning synchrotron imaging techniques to investigate this further. Thin sections of 1 cm × 1 cm × 30 μm dimensions of modern stromatolite
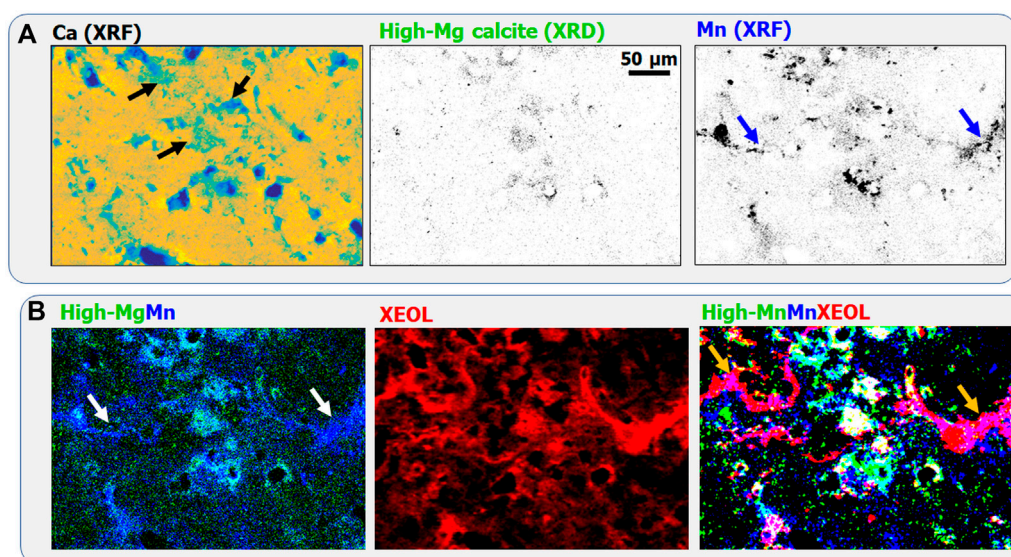
FIGURE 2
(A) Calcium distribution obtained by XRF (shown in "Parula" colormap for better visibility), high-magnesium calcite identified by XRD, and Mn distribution obtained by XRF. In the low-Mg calcite and Mn maps darker pixels indicate larger concentrations. **(B)** High-Mg calcite ("High-Mg" green)-Mn (blue) RGB map, XEOL luminescence distribution, and high-Mg calcite (green)-Mn (blue)-XEOL (red) RGB map. Pixel size is 1 μm, the acquisition time is 40 ms/pixel.

samples were prepared for synchrotron measurements. The multimodal scanning imaging experiments were performed at 18.3 keV X-ray energy. Sample regions measuring between several hundreds of μm² and a few mm² in size have been measured with a 1 μm pixel size and 40 ms/pixel dwell time. Since biological and geological samples naturally contain a variety of endogenous fluorescent molecules, scanning XEOL was chosen in combination with XRF and XRD for multimodal imaging. Simultaneous collection of XRF, XEOL, and XRD produced overlay imaging of the complementary modalities with the same probing spatial resolution. Simultaneous XRD and XRF imaging permitted to identify major and minor crystalline phases in the stromatolites together with their trace element content.

Scanning XRF spectrometry of the measured stromatolite region reveals that Ca can be found throughout the whole sample region (Figure 2A). Simultaneous scanning XRD permitted to identify low-magnesium calcite as a major mineral phase with ~6% MgCO₃. No aragonite could be detected in the measured sample region. High-magnesium calcite, containing ~13% MgCO₃, was identified as a minor crystalline phase distributed in certain locations (Figure 2A). Such variations in the Mg content of calcite were consistently detected by Debrie et al., 2022. Here, we also observed that Mn can be found as a trace element with inhomogeneous distribution within the measured sample area. Interestingly, the colocalization of high-Mg calcite ("High-Mg" in green) and Mn (blue) within the cyan regions of the RGB map (Figure 2B) indicates that all high-Mg calcite regions are enriched in Mn. However, Mn-rich regions can also be found within low-Mg calcite (marked, e.g., by blue and white arrows in the Mn and (High-Mg)Mn RGB maps, respectively). Both high-Mg and low-Mg calcite emits intense red luminescence in Mn-rich regions as shown by the XEOL map and by the white, and violet regions, respectively in Figure 2B. This indicates that Mn(II), a luminescence activator, is likely incorporated into the (Mg,Ca) CO₃

crystal lattice. It can be noted that the scarce micron-scale high-magnesium calcite phase regions might not be detectable by bulk XRD. However, even ppm quantity of Mn incorporated into the crystal lattice will provide an intense red luminescence signal detectable by laboratory luminescence methods.

Another minor crystalline phase, micro-crystalline arsenopyrite, has been identified by XRD and XRF (see Figure 3A). These tiny FeAsS crystals are also enriched in Mn (see Mn distribution in Figure 2B). Comparing the distributions of FeAsS, S, and Fe reveal that FeAsS is the only S-rich phase in the measured sample region. By contrast, most of the tiny Fe-rich features are not linked with arseno-pyrite or other sulfur-bearing mineral phases. The scarce FeAsS crystals corresponding to the cyan regions in the XEOL-Fe-Pyrite RGB map (Figure 3B) do not emit detectable luminescence: Fe(II) is a luminescence inhibitor. Green, Fe-rich, non-luminescing regions suggest the presence of divalent Fe(II) incorporated into the lattice of low-Mg calcite. Scarce yellow regions, containing significantly lower Fe than the Fe-rich hot-spots and FeAsS micro-crystals, are Fe-containing luminescing phases. Part of these is arranged in filament-like structures (white and blue arrows in the RGB and Fe-distribution maps, respectively). In these yellow regions, the presence of Fe(III), a luminescence activator, can be supposed. By contrast, diffuse Fe-containing regions marked by orange arrows in the bottom of the XEOL-Fe-Pyrite RGB map do not emit luminescence.

3.2 Pathological calcification

Pathological biomineralization, including atherosclerosis, osteo-malacia, osteo-porosis, and urolithiasis have a significant impact on human health. For example, kidney stone formation affects ~10–20% of the population worldwide. As such, the
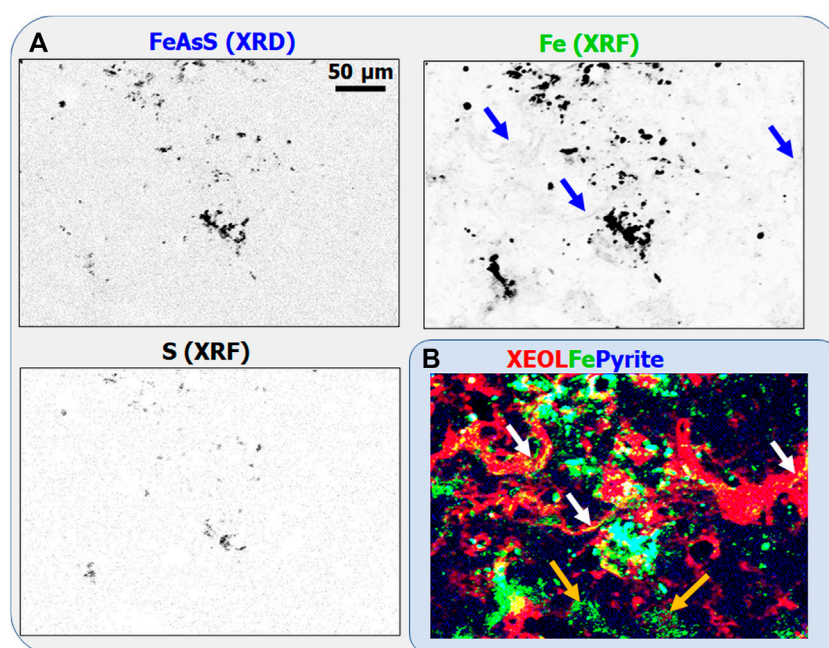
FIGURE 3
(A) FeAsS crystalline phase identified by scanning XRD, together with Fe and S distributions determined by XRF. Darker points correspond to larger concentrations. **(B)** XEOL (red)-Fe (green) -Pyrite (blue) RGB map.

development of broadly effective treatment and prevention have high societal impact. This requires the thorough understanding of the causes and physiological processes triggering and maintaining urolithiasis and the underlying diagenetic phase transition processes. However, the biologically controlled physicochemical processes resulting in kidney stone formation are still poorly understood. It is generally accepted that tissular calcification processes occurring within the renal papillae play a major role in the formation of urinary stones (Randall, 1936; Khan et al., 2016). Namely, a substantial number, approximately one-third, of idiopathic Ca-oxalate stones are forming attached to calcium phosphate plaques, called Randall's plaque (RP) (Randall, 1936; Chi et al., 2015; Khan et al., 2016), forming at the tip of renal papillae. However, the common presence of RP's in non-stone formers (Bird and Khan, 2017) indicates that not all RP's trigger stone formation. Thus, the study of early calcification within renal papillae seems to be a crucial step towards the comprehensive understanding of biologically controlled stone formation.

Essential trace metals are intrinsic components of numerous biological systems including about one-third of all known proteins, which contain metal cofactors as catalytic components (McCall et al., 2000). Thus, it is likely, that some of these elements may also play an important, however not yet understood, role in early pathological calcification processes. For example, recent studies (Chi et al., 2015; Ramaswamy et al., 2015; Negri, 2018) report that renal papillae and Randall's Plaque are enriched in Zn, suggesting that this essential trace metal might play a role or be linked to early calcification processes. Gaining insight into the role of Zn (and other essential trace metals) in the underlying pathophysiology of early stone formation necessitates the simultaneous study of major and trace elements at multi-length scales in tissular, cellular, and

subcellular context. However, such studies have not been performed yet, according to our knowledge. Multimodal scanning hard X-ray imaging and tomography providing access to information on the hierarchical organization of early biocalcification from tissular down to subcellular level can tackle this challenge. Indeed, simultaneous scanning X-ray Fluorescence (XRF), X-ray Diffraction (XRD), and absorption contrast imaging/tomography provide an efficient tool to identify unambiguously early calcification structures and study their morphology, crystalline phase, and trace element content as a unique complement to full field μ-tomography and other laboratory techniques.

Here we present the results obtained on renal papillea samples collected from genetically modified Abcc6−/−mice. This animal model mimics effectively human calcification disorders while reducing biological variability. Indeed, the lack of ABCC6 gene can lead to increased calcium phosphate (CaP) precipitation promoting calcification and Randall plaques formation (Letavernier et al., 2016). The investigated papillae samples were preserved in a 4% formaldehyde solution and embedded in paraffin. Thin tissue sections have been cut by a microtome (Microm HM340E, Thermo Scientific) and placed on a silicon nitride membrane of 3 mm × 3 mm dimensions for synchrotron studies.

As a first step, we measured mesoscale regions with (sub-) micron resolution to gain an overall insight into the calcification features in tissular context. In Figure 4A, the simultaneously measured absorption contrast (Abs), Ca, and Zn distributions are shown within a H x V = 358 μm × 373 μm region of a 50 μm thick mouse renal papillae slice. The Ca and Zn distributions reveal that Ca and Zn are present within the whole tissue of the renal papillae. Highly calcified features correspond to darker regions in the absorption contrast, Ca, and Zn distribution maps. These highly
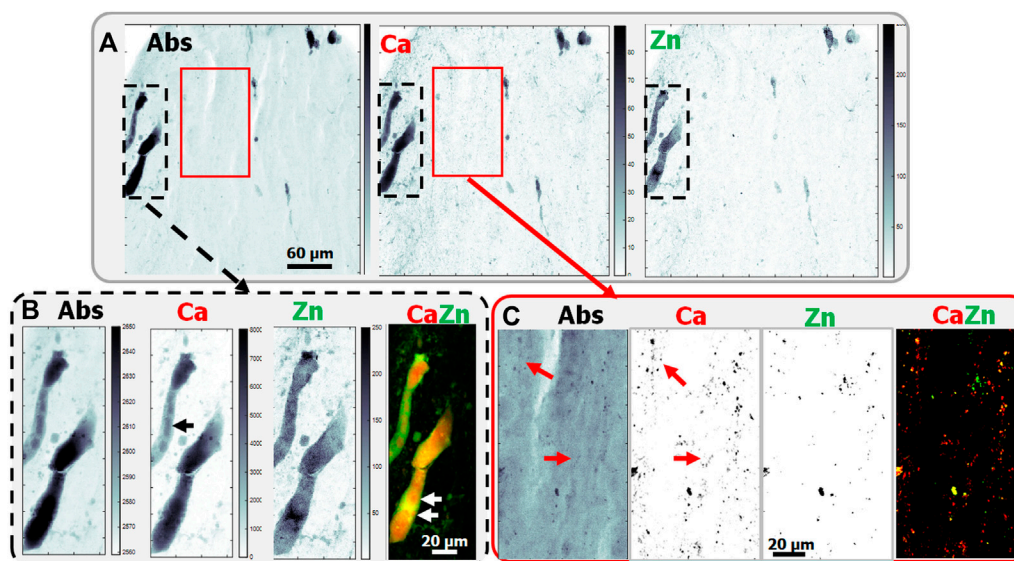
FIGURE 4
(A) Absorption contrast, Ca, and Zn distributions within a 358 μm × 373 μm (H x V) sample region of a 50 μm thick mouse renal papillae, pixel size 400 nm. In the absorption contrast image darker color corresponds to larger density. In the Ca and Zn distribution maps, darker color corresponds to larger concentrations. For better visibility the square root of the Ca intensity is shown in the Ca map. **(B)** Enlarged region containing the tubular calcifications marked by the dashed black square in image **(A)**. **(C)** Enlarged image of the sample region marked by red rectangle in image **(A)**, containing interstitial calcifications. In the RGB false color map Ca is indicated in Red, Zn in Green. Yellow regions correspond to Ca-Zn colocalization.

calcified areas, such as the one outlined with a black rectangle, are typical tubular calcifications containing 20–30-fold Ca and 4-5-fold Zn than the surrounding tissue. The enlarged region (black rectangle in Figure 4A) containing the large tubular calcifications (Figure 4B) reveals that they are composed of agglomerations of smaller, some tens of micron sized, dense Ca-rich fragments. Although Zn is colocalized with Ca within these tubular calcifications, their spatial distributions within the tubes are different: the Zn distribution is more homogenous than that of Ca. The Ca-Zn false color map suggests that a part of Zn is likely deposited along the tube walls and as such, englobes the deca-micron sized calcifications enclosed within the tubes. However, for unambiguous conclusion 3D information is necessary.

Next to tubular calcifications, tiny, interstitial, early calcifications can also be distinguished, as shown in the zoom-in images (Figure 4C), corresponding to the red rectangle in Figure 4A. Thanks to the high analytical sensitivity of XRF, the Ca distribution map provides better contrast for identifying (sub-)micron sized calcification features (e.g., red arrows), which are hardly or not visible in the absorption contrast image. In contrast to tubular calcifications, only part of these early calcifications contains increased Zn content. Moreover, while the Zn-rich regions are always in the vicinity of calcification-rich regions, they do not always contain Ca (see Ca-Zn RGB map).

Scanning XRF and multimodal tomography was used to get further information on the above-described features. Thanks to the relatively large, 50 μm, sample thickness compared to the size of the tubular and interstitial calcifications, these non-invasive tomography techniques preserve the localization and morphology even of tiny calcification features at tissular, cellular, and sub-cellular level. The 3D volume rendering of the Ca and Zn distributions

obtained by sparse XRF tomography in the same region as the region shown in Figure 4, can be seen in Figures 5A,B. This confirms the presence of a Zn-rich layer, which, on one hand, is deposited along the wall of the conducting tubes and on the other hand covers the surface of tubular calcifications (see cut-off view of the tubes in Figure 5B). The tubular calcifications contain about 50% less Zn than these Zn-rich layers. Comparing the 400 nm resolution 2D projection images (Figure 4) and the 3D sparse tomography results (Figures 5A,B) reveals that the smallest, earliest, calcification features having some micrometer-sized dimensions cannot be detected by sparse tomography due to the limited, ~8 μm, spatial resolution. However, such sparse tomography provides a valuable tool for obtaining an overview information about calcification formation in tissular and sub-organ context, and to choose the altitudes for high-resolution (HR) single slice scanning tomography. In Figure 5C the reconstructed HR tomography slices, measured at the positions marked by 1–3 in Figure 5A with 1 μm resolution, are shown. In order to reveal the position of the tiny calcification features within the single slices, the Compton scattering tomogram was also reconstructed from the XRF spectra. HR single slice tomography confirms that most tubular calcifications (white arrows) are covered by a thin Zn layer. Thanks to the improved, 1 μm resolution, the thickness of this Zn-rich layer can also be measured (~1–3 μm). An almost perfect Zn-covered spherical early tubular calcification of ~8 μm diameter can be identified in the middle of Slice 1 (white arrow in Figure 5C in the middle of the slice).

Micro-meter-sized interstitial calcifications are distributed throughout the renal papillae tissue as shown by, e.g., red arrows in the different virtual slices shown in Figure 5C. These tiny, calcified regions contain varying Ca to Zn ratio indicated by the varying
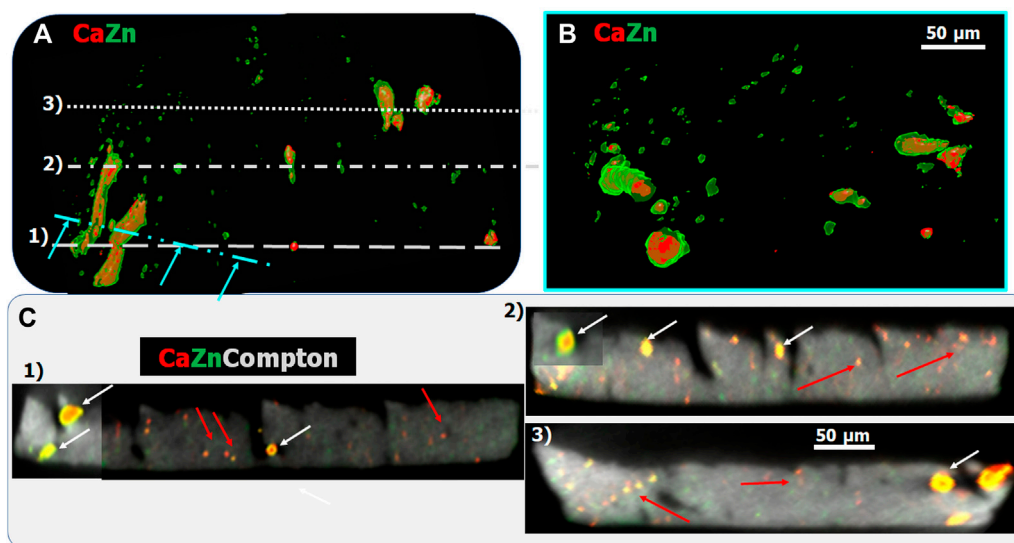
FIGURE 5
(A,B): Volume rendering of the Zn (green) and Ca (red) 3D sparse tomograms of the sample shown in Figure 4. **(B)** shows the cut-off view along the cyan dash-dotted line indicated in **(A)** revealing the internal structure of the tubular calcifications. **(C)** High, 1 µm, resolution single slice tomography measured along the lines marked by 1–3 in **(A)**. Red arrows indicate interstitial calcification, while white arrows show tubular calcifications.
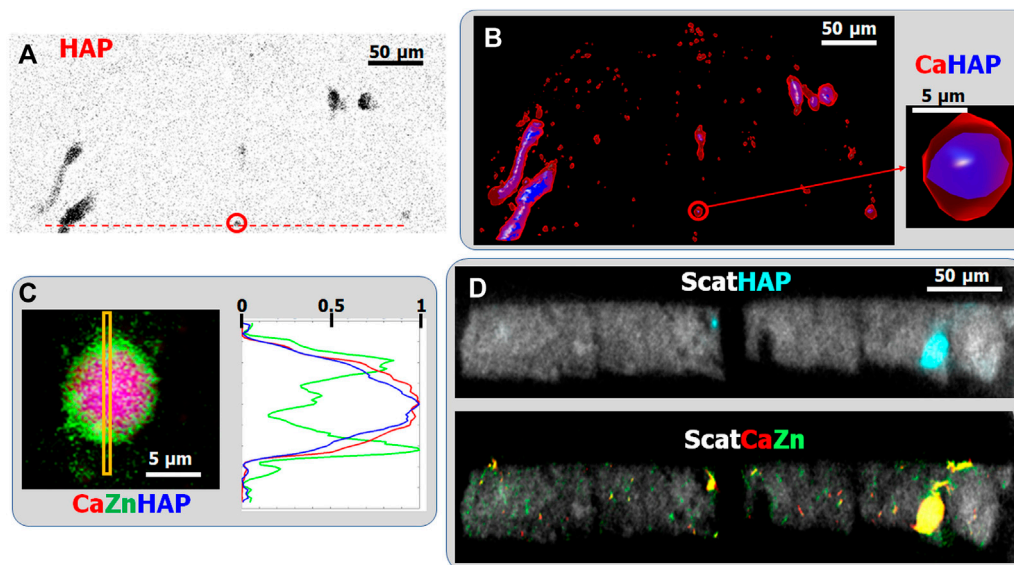

FIGURE 6
(A) Nanocrystalline hydroxyapatite (HAP) distribution within the investigated mouse papillae slice obtained by 2D scanning XRD with 1 µm spatial resolution. **(B)** Volume rendering of Ca (red) and HAP (blue) distributions, obtained by sparse XRF and XRD multimodal tomography. Resolution is ~8 µm. **(C)** Highly resolved (pixel size: 150 nm) projection images of the Ca (Red), Zn (green), and HAP (blue) distributions within the ~8 µm sized Ca-rich sphere marked by red circle (enlarged image) in **(B)**. **(D)** HR single slice multimodal XRF-XRD tomography: scattering (Gray), Ca (red), Zn (green), and HAP (cyan). Spatial resolution: 1 µm.

colors from green (highest Zn to Ca ratio) to red (lowest or no Zn content) in the RGB maps.

To obtain information about the crystalline phases and their spatial distribution, we used simultaneous multi-length-scale XRF-XRD projection imaging, sparse 3D tomography, and HR single slice tomography. Both sparse XRD tomography (8 µm resolution) and XRD projection imaging (1 µm resolution) reveal the presence of

nano-crystalline hydroxy-apatite (HAP) within tubular calcifications (Figures 6A,B). In Figure 6C the high, 150 nm, spatial resolution RGB distribution of Ca (Red), Zn (green), and HAP (blue) of the 8 µm diameter Ca-rich sphere is shown. The mean profile of the Ca, HAP, and Zn distribution within the yellow rectangle shows the presence of Zn within the nano-HAP containing sphere. An about 2-3-fold Zn enrichment within the
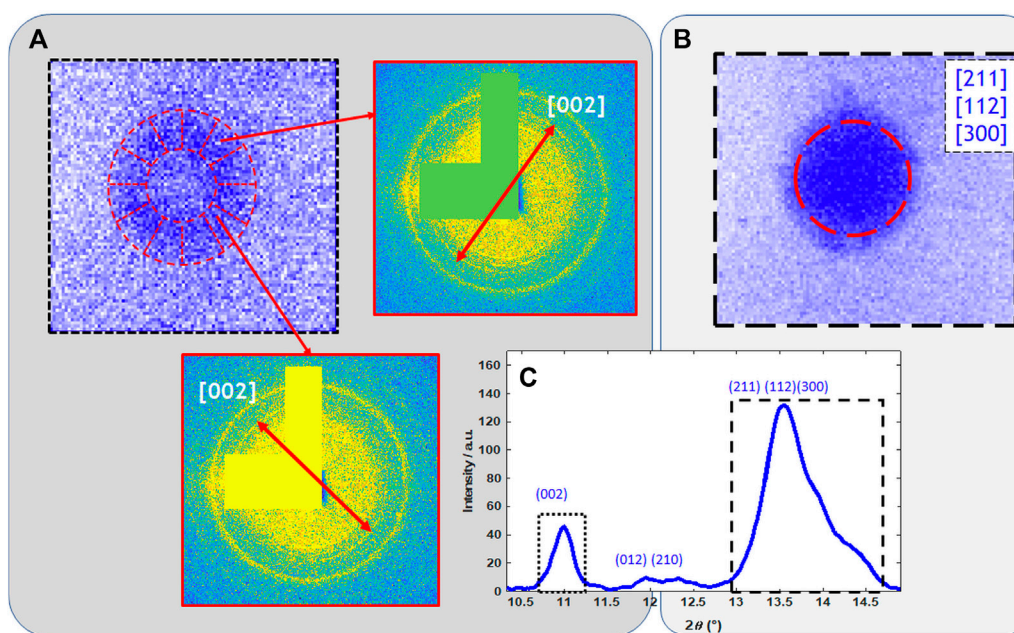
FIGURE 7
(A) Measured intensity distribution of the [002] diffraction peak of the nano-HAP within the ~8 µm sized Ca-rich sphere marked by red circle (enlarged image) in Figure 6B. Annular segmented region of interest allows to highlight the preferential orientation observed on the diffraction patterns. **(B)** Measured homogenous intensity distribution of the [211] [112] [300] diffraction peaks. **(C)** Sum diffractogram within the nano-HAP sphere.

0.75–1 µm thick non-crystalline surface layer can be observed. The angular orientation of the 2D XRD patterns of the outermost crystalline layer, situated just under the Zn-rich layer, reveals the presence of plate-like tangentially oriented crystallites (Figure 7) (Miyabe et al., 2007; Lee et al., 2020) on the surface of the small calcification sphere. Figures 7A,B show the XRD pattern of two single ROI's at 90° distance from each other along the phi axis.

On the other hand, no crystalline phase could be detected in (sub-)micron sized interstitial calcifications, neither with sparse XRD tomography nor with 2D XRD projection imaging. This was corroborated by extracting the sum-diffractogram within a mask, obtained from the Ca-distribution map of the interstitial calcification regions. Furthermore, HR single slice multimodal XRF-XRD tomography confirmed this observation providing the internal distribution of HAP and Ca (Figure 6D). Only the larger, tubular calcifications contain nanocrystalline HAP. This finding suggests that in the early phase of calcification, the first emerging Ca-bearing mineral phases are mostly amorphous (likely calcium phosphate). However, since the analytical sensitivity of XRD is more than two orders of magnitude worse than that of XRF, this observation must be confirmed by further investigations. The detailed high-resolution 3D tomography of such tiny individual internal sample features can be obtained by local tomography, as we have illustrated in a previous paper in the case of XRF tomography (Guo et al., 2022).

4 Discussion and conclusion

The study of geological and paleo-biological systems, such as stromatolites, and the confirmation of biogenicity, necessitates the use of multiple complementary approaches in different length- and

sensitivity scales. Here, we used high-resolution multimodal XRF-XRD-XEOL projection imaging to study modern stromatolites from the coastal Mari Ermi lagoon. The high analytical sensitivity of synchrotron radiation excited nano-X-Ray Fluorescence (compared to electron microscopy) permitted to reveal, with high spatial resolution, the distribution, and concentration variation of Mn and Fe in the [ppm, 0.1 %] and [ppm, 1%] concentration ranges, respectively. The colocalization of Fe, Mn, and XEOL revealed that the main luminescence activator in the measured sample region is Mn(II). Mn-rich red luminescence emitting regions are situated both within low-Mg and high-Mg calcite phases, suggesting that the incorporation of bivalent Mn(II) into calcite is not linked linearly to their Mg content. The studied 625–675 nm wavelength range of the XEOL spectrum covers the fluorescence emitted by photosynthetic pigments chlorophylle/phycocyanine enclosed in the organic material of the stromatolite (Debrie et al., 2022) and also the high-wavelength tail of the Mn(II)-substituted calcite fluorescence. As a next step, further multimodal X-ray imaging measurements are foreseen by implementing a high spectral resolution XEOL spectrometer, to be able to identify unambiguously the presence and spatial distribution of photosynthetic pigments within the magnesian-calcite and to explore their chemical composition.

The scanning multimodal X-ray imaging study of Abcc6-mice renal papillae samples highly profited from the high analytical sensitivity of SR-nano-XRF for revealing the trace level presence of Ca and Zn within the tissue of the mouse renal papillae. The possibility to analyze meso-scale regions (0.5 mm dimensions) of the renal papillae with 400 nm spatial resolution provided the possibility to compare tubular and interstitial calcifications with high statistical significance. Tubular calcifications are dense, some tens of

micrometer sized biominerals, containing nano-crystalline hydroxyapatite (HAP) with no other detectable crystalline phases. Larger tubular calcifications are created by agglomeration. All the measured tubular calcifications are enriched in Zn, containing 4–5 times more Zn than the surrounding tissue. The distribution of Zn within tubular calcifications at the nanometer scale is highly heterogenous. High-resolution scanning XRF tomography was crucial to identify unambiguously the thin, (sub-)micron Zn-rich surface layers on micron-scale calcification features and along tube walls. These contain up to 2–3 times higher Zn than the HAP core. The spherical shape and successive layers containing different Zn to Ca ratios indicate successive dissolution and re-crystallization processes during crystal formation. Tiny (≤3–4 μm) interstitial calcification have been found all over the renal papillae, containing no crystalline phases within the detection limit of nano-XRD. This suggests that they are composed mostly of amorphous, likely Ca-phosphate minerals. This will be checked by further measurements on other samples. Only about 50% of the interstitial calcifications do contain up to 2-3-folds higher Zn than the surrounding tissue. This finding suggests that Zn is not involved in the nucleation process of early calcification.

The study of two biomineral systems detailed above, illustrates the figure-of-merit of the straightforward and flexible implementation of different analytical modalities in scanning hard X-ray integrative imaging. Moreover, the high penetration depth of hard X-rays and the easily tunability of the probed field-of-view open the way towards multi-length-scale studies both by 2D projection imaging and 3D scanning tomography. Non-invasive scanning X-ray multimodal imaging and tomography can span over six orders of magnitude length-scales bridging the gap between meso-scale samples of some millimeter dimensions and tiny nanometer sized internal sample features. Such a versatile portfolio of X-ray imaging techniques can provide unique information and is complementary to conventional laboratory techniques, especially on the role and effect of minor and trace elements on the biomineralization process. Indeed, biominerals, even when formed under similar conditions, often show a different elemental composition compared to inorganic precipitates, a phenomenon which is not fully understood yet.

The flexible combination of different analytical modalities provides an efficient tool to tailor the analytical possibilities to the scientific challenge. For example, XEOL can provide fast qualitative simultaneous information on the valence states of several elements in specific mineralogical context and can also indicate potential radiation damage in case of radiation sensitive chemical components. This can be an interesting figure-of-merit compared to the slow and photon-hungry, radiation damage sensitive XANES imaging, which on the other hand has the advantage of providing precise, quantitative information on the local chemical environment of the investigated elements.

From a methodological point of view, simultaneous measurement of all modalities has particular importance in producing overlay imaging with the same probing spatial resolution. Such integrative multimodal imaging approach is still in its infancy (Callefo et al., 2022; Graziotto et al., 2023). It permits to combine all information to study highly heterogenous systems in a more quantitative manner and with higher sensitivity. For example, the high (ppm) analytical sensitivity of

XRF is a crucial requirement to be able to detect the earliest calcification features in biological samples (through the detection of Ca). Indeed this is not available by XRD due to its worse (~%) detection limit. On the other hand, XRD can reveal the presence, distribution, and concentration variation of major light elements contained in main crystalline phases, which are usually not detectable at scanning hard XRF set-ups (e.g., Mg in magnesian-calcite). This pushes further the precision of the elemental quantification obtained by XRF. A particular technical challenge is to integrate simultaneously all the necessary detectors within the tight space available at scanning hard X-ray nanoprobes around the sample. NANOSCOPIUM intends to tackle this challenge by integrating a new dedicated XEOL spectrometer in the X-ray beam path in reflection geometry in front of the sample, to be able to perform simultaneous XRF-XEOL-XRD measurements in the future.

Emerging multi-length-scale scanning tomography techniques and their combination into an integrative multimodal approach provide invaluable tools for the study of biomineralizations. However, high-resolution 3D tomography of mesoscale samples is not feasible at third generation synchrotron sources due to the long measurement times (up to 24 h). The upgrade of 3rd generation sources (which is under consideration at Synchrotron Soleil) and emerging 4th generation synchrotron sources will bring these HR scanning 3D tomography techniques within reach for standard user experiments.

Data availability statement

The raw data supporting the conclusion of this article will be made available by the authors, without undue reservation.

Ethics statement

The animal study was approved by the Health Ministry and local Ethics Committee (authorization 11420 2017092015335292). The study was conducted in accordance with the local legislation and institutional requirements.

Author contributions

KM: Investigation, Methodology, Software, Writing–review and editing. KB: Investigation, Validation, Writing–review and editing. Juliette JD: Investigation, Methodology, Writing–review and editing. ET: Investigation, Methodology, Writing–review and editing. DB: Investigation, Writing–review and editing. EL: Investigation, Writing–review and editing. KD: Investigation, Methodology, Writing–review and editing. AS: Investigation, Methodology, Writing–original draft, Writing–review and editing.

Funding

Acknowledgments

Conflict of interest

The authors declare that the research was conducted in the absence of any commercial or financial relationships that could be construed as a potential conflict of interest.

The handling editor MPI declared a past co-authorship with the authors KM and AS.

Publisher's note

All claims expressed in this article are solely those of the authors and do not necessarily represent those of their affiliated organizations, or those of the publisher, the editors and the reviewers. Any product that may be evaluated in this article, or claim that may be made by its manufacturer, is not guaranteed or endorsed by the publisher.

References

AXO (2024). *Thin film XRF reference sample.* https://www.axo-dresden.de/en/products/reference-samples.

Bazin, D., Daudon, M., Combes, C., and Rey, C. (2012). Characterization and some physicochemical aspects of pathological microcalcifications. *Chem. Rev.* 112, 5092–5120. doi:10.1021/cr200068d

Bazin, D., Letavernier, E., and Jph, H. (2016). Biomineralization versus microcrystalline pathologies: beauty and the beast. *C. R. Chim.* 19, 1395–1403. doi:10.1016/j.crci.2015.12.012

Bird, V. Y., and Khan, S. R. (2017). How do stones form? Is unification of theories on stone formation possible. *Arch. Esp. Urol.* 70, 12–27.

Bosak, T., Knoll, A. H., and Petroff, A. P. (2013). The meaning of stromatolites. *An. Rev. Earth Planet. Sci.* 41, 21–44. doi:10.1146/annurev-earth-042711-105327

Callefo, F., Ricardi-Branco, F., Alves Forancelli Pacheco, M. L., Cardoso, A. R., Noffke, N., de Carvalho Teixeira, V., et al. (2022). Evidence for metabolic diversity in meso-neoproterozoic stromatolites (vazante group, Brazil). *Front. Earth Sci.* 10, 163–172. doi:10.3389/feart.2022.804194

Chi, T., Kim, M. S., Lang, S., Bose, N., Kahn, A., Flechner, L., et al. (2015). A Drosophila model identifies a critical role for zinc in mineralization for kidney stone disease. *PLoS ONE* 10 (5), e0124150. doi:10.1371/journal.pone.0124150

Chu, Y. S., Lee, W. L., Tappero, R., Ge, M., Huang, X., Xiao, X., et al. (2020). Multimodal, multidimensional, and multiscale X-ray imaging at the national synchrotron light source II. *Synchrotron Radiat. News* 33, 29–36. doi:10.1080/08940886.2020.1751520

Debrie, J., Prêt, D., Menguy, N., Estève, I., Sans-Jofre, P., Saint Martin, J. P., et al. (2022). Mapping mineralogical heterogeneities at the nm-scale by scanning electron microscopy in modern Sardinian stromatolites: deciphering the origin of their laminations. *Chem. Geol.* 609, 121059. doi:10.1016/j.chemgeo.2022.121059

Epstein, C. L. (2008). *Introduction to the mathematics of medical imaging.* Philadelphia: SIAM Edition.

Gaft, M., Reisfeld, R., and Panczer, G. (2015). *Modern luminescence spectroscopy of minerals and materials.* Switzerland: Springer Mineralogy.

Görgen, S., Benzerara, K., Skouri-Panet, F., Gugger, M., Chauvat, F., Cassier-Chauvat, C., et al. (2021). The diversity of molecular mechanisms of carbonate biomineralization by bacteria. *Discov. Mater* 1, 2. doi:10.1007/s43939-020-00001-9

Graziotto, M. E., Kidman, C. J., Adair, L. D., James, S. A., Harris, H. H., and New, E. J. (2023). Towards multimodal cellular imaging: optical and X-ray fluorescence. *Chem. Soc. Rev.* 52, 8295–8318. doi:10.1039/d3cs00509g

Guo, R., Somogyi, A., Bazin, D., Bouderlique, E., Letavernier, E., Curie, C., et al. (2022). Towards routine 3D characterization of intact mesoscale samples by multi-scale and multimodal scanning X-ray tomography. *Sci. Rep.* 12, 16924. doi:10.1038/s41598-022-21368-0

Hunter, D. R., and Lange, K. (2004). A tutorial on MM algorithms. *Am. Stat.* 58, 30–37. doi:10.1198/0003130042836

Iniesto, M., Moreira, D., Reboul, G., Deschamps, P., Benzerara, K., Bertolino, P., et al. (2021). Core microbial communities of lacustrine microbialites sampled along an alkalinity gradient. *Env. Microbiol.* 23, 51–68. doi:10.1111/1462-2920.15252

Khan, S. R., Pearle, M. S., Robertson, W. G., Gambaro, G., Canales, B. K., Doizi, S., et al. (2016). Kidney stones. *Nat. Rev. Dis. Prim.* 2, 16008. doi:10.1038/nrdp.2016.8

Lee, S., Nagata, F., Kato, K., and Nakano, T. (2020). Bone apatite anisotropic structure control via designing fibrous scaffolds. *RSC Adv.* 10, 13500–13506. doi:10.1039/d0ra01295e

Letavernier, E., Bazin, D., and Daudon, M. (2016). Randall's plaque and kidney stones: recent advances and future challenges. *Comptes Rendus Chim.* 19, 1456–1460. doi:10.1016/j.crci.2014.12.005

Martínez-Criado, G., Alén, B., Sans, J. A., Lozano-Gorrín, A. D., Haro-González, P., Martín, I. R., et al. (2017). X-ray nanoimaging of Nd3+ optically active ions embedded in Sr_05Ba_05Nb_2O_6 nanocrystals. *Opt. Mat. Express* 7, 2424–2431. doi:10.1364/ome.7.002424

McCall, K. A., Huang, C. C., and Fierke, C. A. (2000). Function and mechanism of zinc metalloenzymes. *J. Nutr.* 130, 437S–46S. doi:10.1093/jn/130.5.1437S

Medjoubi, K., Leclercq, N., Langlois, F., Buteau, A., Lé, S., Poirier, S., et al. (2013). Development of fast, simultaneous and multi-technique scanning hard X-ray microscopy at Synchrotron Soleil. *J. Synchrotron. Rad.* 20, 293–299. doi:10.1107/s0909049512052119

Miyabe, S., Nakano, T., Ishimoto, T., Takano, N., Adachi, T., Iwaki, H., et al. (2007). Two-dimensional quantitative analysis of preferential alignment of BAp c-axis for isolated human trabecular bone using microbeam X-ray diffractometer with a transmission optical system. *Mater. Trans.* 48, 343–347. doi:10.2320/matertrans.48.343

NANOSCOPIUM (2024). *The NANOSCOPIUM beamline is open for user proposals.* St Aubin, France: Synchrotron Soleil. https://www.synchrotron-soleil.fr/en/beamlines/nanoscopium.

Negri, A. L. (2018). The role of zinc in urinary stone disease. *Int. Urol. Nephrol.* 50, 879–883. doi:10.1007/s11255-017-1784-7

Pafilis, C., Gaitanis, A., Gatis, C., Kontaxakis, G., Spyrou, G., Panayiotakis, G., et al. (2011). "A methodology for the estimation of the optimal iteration in MLEM-based image reconstruction in PET," in Proceedings of the 10th International Workshop on Biomedical Engineering, Kos, Greece, October 2011 (IEEE), 1–4. doi:10.1109/IWBE.2011.6079046

Parsons, A. D., Price, S. W. T., Wadeson, N., Basham, M., Beale, A. M., Ashton, A. W., et al. (2017). Automatic processing of multimodal tomography datasets. *J. Synchrotron. Rad.* 24, 248–256. doi:10.1107/s1600577516017756

Pettersen, E. F., Goddard, T. D., Huang, C. C., Couch, G. S., Greenblatt, D. M., Meng, E. C., et al. (2004). UCSF Chimera: a visualization system for exploratory research and analysis. *J. Comput. Chem.* 25, 1605–1612. doi:10.1002/jcc.20084

Putz, H., and Brandenburg, K. (2024). Match!- phase analysis using powder diffraction. Version 3.x, crystal impact. *GbR, Kreuzherrenstr.* 102, 53227. https://www.crystalimpact.de/match/references.htm.

Quinn, P. D., Alianelli, L., Gomez-Gonzalez, M., Mahoney, D., Cacho-Nerin, F., Peach, A., et al. (2021). The hard X-ray nanoprobe beamline at diamond light source. *J. Synch. Rad.* 28, 1006–1013. doi:10.1107/s1600577521002502

Ramaswamy, K., Killilea, D. W., Kapahi, P., Kahn, A. J., Chi, T., and Stoller, M. L. (2015). The elementome of calcium-based urinary stones and its role in urolithiasis. *Nat. Rev. Urol.* 12, 543–557. doi:10.1038/nrurol.2015.208

Randall, A. (1936). An hypothesis for the origin of renal calculus. *N. Engl. J. Med.* 214, 234–242. doi:10.1056/nejm193602062140603

Saint Martin, J. P., and Saint Martin, S. (2015). Discovery of calcareous microbialites in coastal ponds of western Sardinia (Italy). *Geo-Eco-Marina* 21, 35–53.

Schindelin, J., Arganda-Carreras, I., Frise, E., Kaynig, V., Longair, M., Pietzsch, T., et al. (2012). Fiji: an open-source platform for biological-image analysis. *Nat. Methods* 9, 676–682. doi:10.1038/nmeth.2019

Schroer, C. G., Baumbach, C., Döhrmann, R., Klare, S., Hoppe, R., Kahnt, M., et al. (2016). Hard x-ray nanoprobe of beamline P06 at PETRA III. *AIP Conf. Proc.* 1741, 030007. doi:10.1063/1.4952830

Sham, T. K. (2014). Photon-in/photon-out spectroscopic techniques for materials analysis: some recent developments. *Adv. Mat.* 26, 7896–7901. doi:10.1002/adma.201304349

Solé, V. A., Papillon, E., Cotte, M., Walter, P., and Susini, J. (2007). A multiplatform code for the analysis of energy-dispersive X-ray fluorescence spectra. *Spectrochim. Acta Part B* 62, 63–68. doi:10.1016/j.sab.2006.12.002

Somogyi, A., Medjoubi, K., Baranton, G., Le Roux, V., Ribbens, M., Polack, F., et al. (2015). Optical design and multi-length-scale scanning spectro-microscopy possibilities at the Nanoscopium beamline of Synchrotron Soleil. *Soleil. J. Synchrotron Radiat.* 22, 1118–1129. doi:10.1107/s1600577515009364

Suuronen, J. P., and Sayab, M. (2018). 3D nanopetrography and chemical imaging of datable zircons by synchrotron multimodal X-ray tomography. *Sci. Rep.* 8, 4747. doi:10.1038/s41598-018-22891-9

Tinti, G., Bergamaschi, A., Cartier, S., Dinapoli, R., Greiffenberg, D., Johnson, I., et al. (2015). Performance of the EIGER single photon counting detector. *J. Instrum.* 10, C03011. doi:10.1088/1748-0221/10/03/c03011

van Heel, M., and Schatz, M. (2005). Fourier shell correlation threshold criteria. *J. Struct. Biol.* 151, 250–262. doi:10.1016/j.jsb.2005.05.009

Yan, H., Bouet, N., Zhou, J., Huang, X., Nazaretski, E., Xu, W., et al. (2018). Multimodal hard x-ray imaging with resolution approaching 10 nm for studies in material science. *Nano Futur.* 2, 011001. doi:10.1088/2399-1984/aab25d

Yan, H., Nazaretski, E., Lauer, K., Huang, X., Wagner, U., Rau, C., et al. (2016). Multimodality hard-x-ray imaging of a chromosome with nanoscale spatial resolution. *Sci. Rep.* 6, 20112. doi:10.1038/srep20112